

An Electrochemical Study on the Impact of Charging Parameters on the Electrochemical Performance of Alloy-Based C/Sn Composite Anodes for Sodium-Ion Batteries

Alexander Kempf,* Philipp Adelhelm, and Magdalena Graczyk-Zajac

The electrochemical performance of C/Sn composite anodes (≈ 11 wt% carbon) for sodium-ion batteries is systematically investigated under varying charging conditions. Galvanostatic cycling with potential limitation reveals a significant influence of charging protocols on capacity and stability. An optimized protocol, starting with a low current (74.4 mA g^{-1}) followed by higher currents (372 mA g^{-1}), achieves a first discharge capacity of 749 mAh g^{-1} , an initial Coulombic efficiency of 84.0%, and a stable capacity of 536 mAh g^{-1} after 100 cycles. A thorough investigation of charge/discharge profiles and incremental capacity analysis reveals a novel, current-induced desodiation process at 0.2 V , enhancing cyclability. Asymmetric cycling reveals

interdependence between sodiation and desodiation, with capacity fading linked to a reaction at 0.26 V . Cut-off potential adjustments allows isolation of individual dealloying processes. The first process at 0.15 V remains stable under varying charging currents, while the second desodiation process ($\approx 0.26 \text{ V}$) transforms from phase transition to solid solution. Long-term cycling identifies potential indicators of performance degradation, which could be mitigated by modifying cycling parameters. An advanced understanding of the complex electrochemical mechanisms in the Na/Sn alloy system is essential for developing protocols to further improve high-capacity anode materials for sodium-ion batteries.

1. Introduction

Sodium-ion batteries (SIB) have recently entered the commercial market with energy densities approaching those of Li-ion technology. A further increase in energy density requires the development of tailored materials with higher capacity. Presently, hard carbons are the anode material of choice for first-generation SIB.^[1–4] A promising strategy to enhance the energy density involves the implementation of an alloy-based charge storage mechanism with high theoretical capacities, employing elements such as Sb, Ge, P, and Sn.^[5] In its fully sodiated state, Sn forms $\text{Na}_{15}\text{Sn}_4$ with an exceptional theoretical capacity of 847 mAh g^{-1} . However, this capacity is accompanied by substantial volume fluctuations of

420% during the (de-)sodiation process and can lead to pulverization and contact loss, which, in turn, can lead to cell failure.^[6,7]

The complex interplay among the various components of the battery system presents a challenge in comprehending its operation, yet concurrently, it unveils numerous avenues for enhancement. First, the structure of the material itself plays a crucial role in the performance. Nanosizing, as well as the use of composite materials, which provide a buffering matrix or porosity to accommodate the volume changes, can help to improve the stability of the materials. Furthermore, the right choice of electrolyte can be pivotal for optimal cell performance.^[8–12] An enhanced comprehension of the electrochemical processes is imperative for ascertaining the optimal working conditions of the cell, especially in multistep reactions, such as during the alloying and dealloying of Sn with Na.

Several research groups have proposed and investigated the electrochemical alloying mechanism of Sn with Na. In early computational works of Chevrier and Ceder in 2011,^[13] the alloying mechanism was proposed as a sequence of four reactions, beginning with the formation of NaSn_5 , NaSn , and Na_9Sn_4 , culminating in the formation of $\text{Na}_{15}\text{Sn}_4$. One year later, Ellis et al.^[14] proposed an alternative mechanism replacing NaSn_5 with NaSn_3 as the initial alloying step. Subsequently, Baggetto et al.^[15,16] suggested a different mechanism, including the formation of unknown and amorphous or nanocrystalline phases. Furthermore, different behaviors and phase formations between the discharging and charging processes have been observed, such as the formation of new plateaus hinting at different reaction pathways. In 2017, another in-depth study backed by pair distribution function analysis, density functional theory, and solid-state nuclear magnetic resonance on

A. Kempf, M. Graczyk-Zajac
Institute of Materials Science
Darmstadt University of Technology
Otto-Berndt-Str. 3, 64287 Darmstadt, Germany
E-mail: alexander_martin.kempf@tu-darmstadt.de

P. Adelhelm
Institute of Chemistry
Humboldt University of Berlin
Brook-Taylor-Str. 2, 12489 Berlin, Germany

M. Graczyk-Zajac
EnBW Energie Baden-Württemberg AG
Durlacher Allee 93, 76131 Karlsruhe, Germany

 Supporting information for this article is available on the WWW under <https://doi.org/10.1002/batt.202500340>

 © 2025 The Author(s). *Batteries & Supercaps* published by Wiley-VCH GmbH. This is an open access article under the terms of the Creative Commons Attribution License, which permits use, distribution and reproduction in any medium, provided the original work is properly cited.

the sodiation mechanism was published by Stratford et al. The proposed mechanism involves a series of new intermediate states and several solid solution reactions, ultimately leading to an even higher sodiated state with composition $\text{Na}_{15+x}\text{Sn}_4$.^[17] This comprehensive investigation was limited to the discharge process and highlighted the importance of kinetics. Zhu et al. have shown that for microsized Sn, the performance is significantly improved by adjusting the upper voltage limit to 0.62 V, avoiding the full desodiation of Sn, which is mainly responsible for surface cracking.^[18] Palaniselvam et al. have reported on the influence of different current rates on the occurring reactions. They also observed a mismatch between the number of intermediate states within sodiation and desodiation, owing to an asymmetric reaction mechanism.^[19] The variety of different observations across various research studies underscores the complexity of the electrochemical (de-)alloying process of the sodium–tin system.

A comprehensive understanding of the complex electrochemical processes of the sodium–tin system is essential, along with material optimization to achieve the best performance for actual applications. This work also elucidates the importance of optimizing working parameters, a field not yet explored in depth, but potentially essential for achieving an electrified future. We investigate a high Sn content C/Sn composite cycled under varying charging conditions. The data is evaluated using a solely electrochemical approach, namely galvanostatic cycling with potential limitation (GCPL), and different data representations such as charge/discharge profiles and incremental capacity analysis (ICA). The focus lies on the effect of different current densities on cycling performance. By applying asymmetric cycling, i.e., galvanostatic cycling at different currents for charging and discharging, as well as exploring different cut-off potentials, we attempt to gain insight into how various electrochemical processes are connected. Finally, the long-term cyclability of an optimized charging protocol is investigated, and early indicators of degradation are discussed.

2. Experimental Section

2.1. Material Synthesis and Electrode Preparation

Fructose was dissolved in a water:ethanol solution (1:9 by weight) before adding SnO_2 nanopowder and mixing it for ≈ 2 h (SnO_2 :fructose $\approx 54:46$ by weight). Subsequently, the solvents were removed, and the resulting sugar/ SnO_2 mixture was placed in an Al_2O_3 crucible within an alumina tube furnace and carbonized at 600 °C for 1 h under argon flow. The obtained C/ SnO_2 composite was crushed by hand, further milled in a ball mill, and sieved to a particle size below 40 μm . The resulting fine powder was heat-treated a second time at 1100 °C for 1 h under argon to carbothermally reduce SnO_2 to metallic Sn. The carbon content of the composite was 10.83 wt%, the remaining composition is primarily Sn; however, small traces of SnO_2 were observed in X-ray diffraction (XRD). This composition was chosen, as it has the highest Sn content, which could be prepared via the carbothermal reduction approach, while still assuring a homogenous distribution of Sn, without large agglomerations (for further information, please refer to our previous work).^[20]

The electrode slurry was prepared using 85 wt% active material and 10 wt% binder (5 wt% Carboxymethyl Cellulose (CMC) and 5 wt% styrene-butadiene rubber (SBR)), and 5 wt% carbon black, with water added to adjust the viscosity. It was then printed on a copper foil using a doctor blade and dried overnight at 40 °C, prior to punching out circular electrodes with a diameter of 10 mm. The electrodes were dried overnight at 80 °C under vacuum and introduced into an argon-filled glovebox.

2.2. Electrochemical Testing

Galvanostatic cycling measurements were conducted in a Swagelok-type half-cell setup, using Na metal as the counter electrode, a quartz microfiber filter QMA separator (Whatman), and 1M NaPF_6 in dimethoxyethane (DME) (Xiamen Tob New Energy Technology Co., LTD) as the electrolyte. The electrochemical tests were carried out on a VMP multipotentiostat (Biologic Science Instruments).

The cells were investigated using different cycling parameters in the GCPL tests. The upper and lower potential limits were set to 0.75 and 0.005 V, respectively. Symmetric and asymmetric cycling was performed. The initial symmetric cycling was performed following three protocols. In the slow protocol (S) a low current density of 74.4 mA g⁻¹ was applied, in the fast protocol (F) the current density was increased to 372 mA g⁻¹, and in the optimized protocol (S + F) an initial cycle was performed at low currents and the following cycles at high currents. In asymmetric cell testing, the first cycle was also carried out using low currents and in the following cycles, either sodiation or desodiation was performed at currents of 372 mA g⁻¹ and the respective other one at low currents (74.4 mA g⁻¹). The S + F cycling was also performed with different cut-off potentials, such as a lower limit of 0.05 V or a higher limit of 0.23 V. The charging protocols are summarized in Figure 1 and Table S1 in the Supporting Information.

The initial Coulombic efficiency (ICE) was calculated as the ratio of the desodiation (charge) capacity to the sodiation (discharge) capacity in the first cycle. The capacity retention in percent was obtained by the division of the capacity after 100 cycles by the initial sodiation capacity.

3. Results

In this work, we primarily focus on the electrochemical analysis of the material. For in-depth information on the material properties, please refer to our previous work.^[20]

GCPL was carried out under varying charging conditions. The cells were cycled either using low current densities of 74.4 mA g⁻¹, high current densities of 372 mA g⁻¹, or with one formation cycle at low and the following cycles at high current densities. These charging protocols are denoted as **slow** (S), **fast** (F), and **slow and fast** (S + F), respectively. The cycling performances are depicted in Figure 2a–c and the associated capacity/voltage profiles in d,e, and f, and the results are

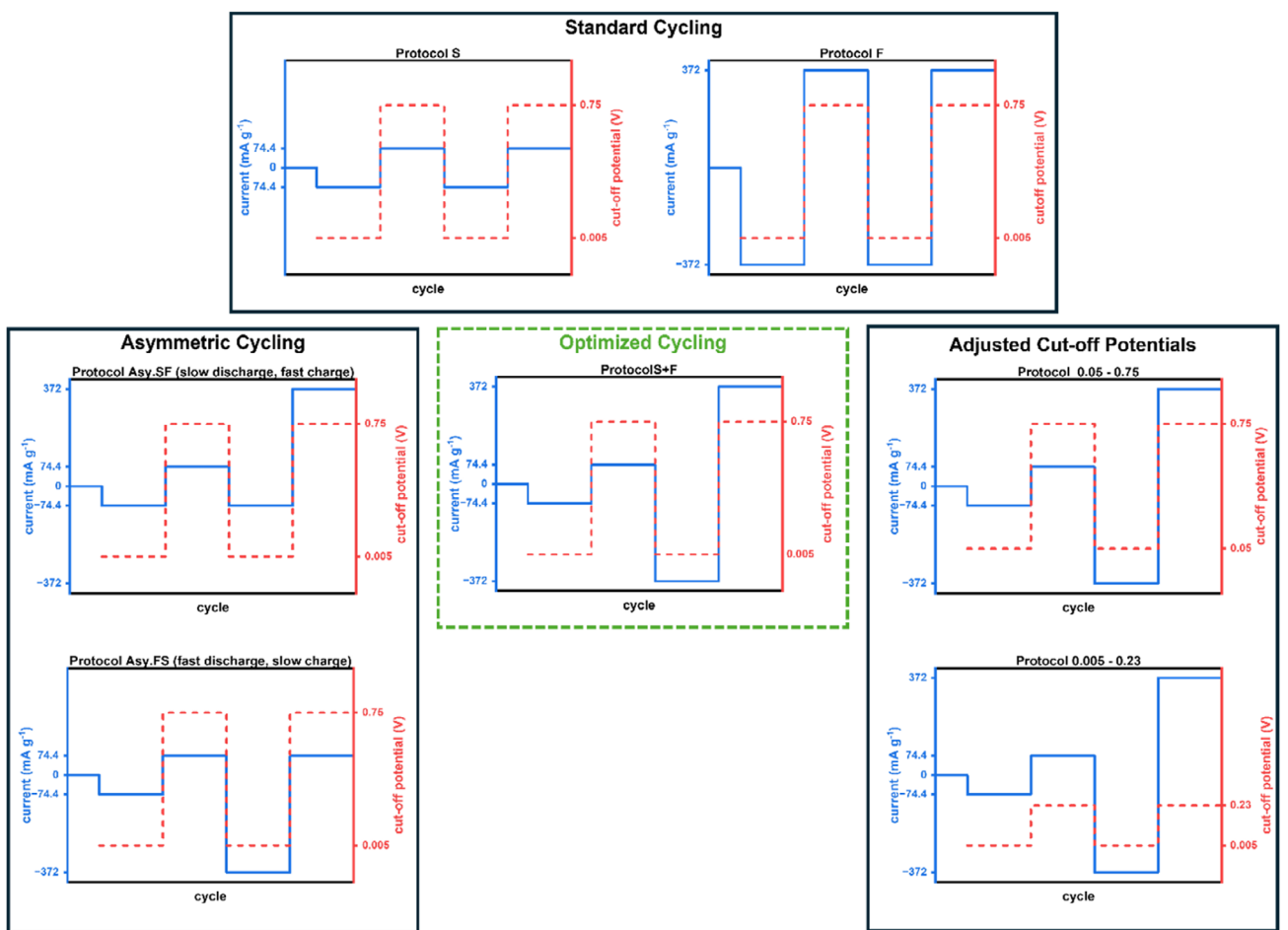


Figure 1. Graphical overview of the different charging protocols employed in this study. The respective current densities (blue) and upper and lower potential limits (red) are indicated. Protocol names are given on top. “S” and “F” denote cycling at slow (74.4 mA g^{-1}) and fast (372 mA g^{-1}) currents. In asymmetric cycling (“S + F”), discharge (sodiation) is done at slow current, and charging (desodiation) is done at fast current. In the optimized cycling, asymmetric cycling, and when the cut-off potentials were adjusted, the initial cycle was carried out at a low current density of 74.4 mA g^{-1} .

summarized in **Figure 3** and Table S2 in the Supporting Information. Table S4 in Supporting Information also compares the performances achieved by the different cycling protocols with various other Sn-based electrodes from the literature. Cycling at the lowest current density results in a continuous fading of the electrochemical performance and from the cell’s original sodiation capacity of 667 mAh g^{-1} , after 100 cycles, merely 259 mAh g^{-1} or 38.8% remain. The sample cycled using a higher current rate of 372 mA g^{-1} shows an initial cycling capacity of 778 mAh g^{-1} with an ICE of 83.9% and no initial continuous fading; however, the recovered capacities are more unstable, especially after around 70 cycles, as reflected in increased variations in efficiencies. Ultimately, after 83 cycles, the capacity starts to drop significantly to 354 mAh g^{-1} . In contrast to the previously discussed, nonoptimal performances, the sample, which was cycled initially with 74.4 mA g^{-1} and then at 372 mA g^{-1} , delivers a high capacity of 536 mAh g^{-1} after 100 cycles along with outstanding cycling stability, achieving efficiencies of $>99\%$ from the fourth to the 100th cycle. During this interval, the mean efficiency is 99.82% and the capacity drops from 555.6 to 534.6 mAh g^{-1} , equal to a remaining

capacity of 96.22% or a decay of 0.040% per cycle. The high CE of the alloy-based anode material will directly lead to the enhancement of the cell CE. While CE of the LIB cells with graphite anode exceeds 99.5% over hundreds of cycles, the CE of alloying anodes (e.g., Si) is less stable and tends to fade. Moreover, the efficiency typically depends on the charge/discharge rate and is lower when it exceeds 0.5 C. These issues are partly tackled, though an alloying anode used, when the S + F protocol is applied.

While the above-discussed capacity-versus-cycle-number plots provide insights into cycling stability, they do not reveal details about specific electrochemical reactions occurring. In contrast, potential versus recovered capacity plots (charge/discharge transients), which are a different way of representing the data of the same GCPL measurement, offer insights into electrochemical reactions taking place. Sloping regions or plateaus in the charge/discharge curves indicate potentials at which capacity is gained, meaning that storage reactions are occurring. Tin-based systems, which store sodium via the formation of various alloys, exhibit multiple plateaus/features in their respective charge/discharge transients, especially during the desodiation process, which will

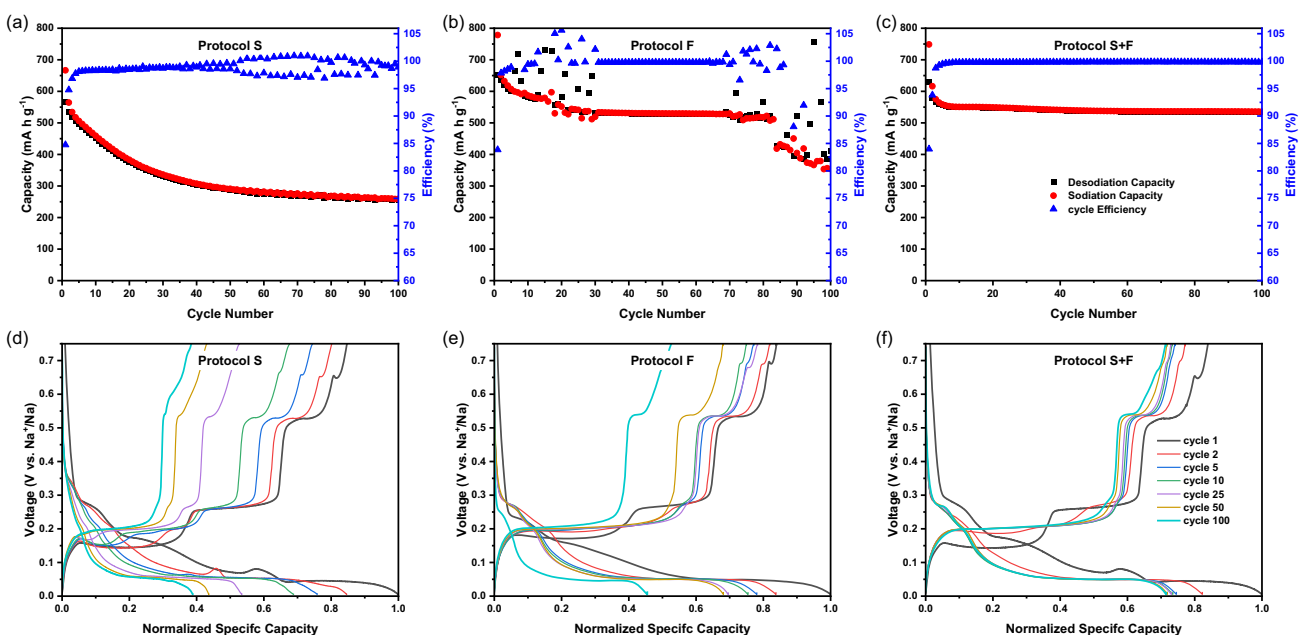


Figure 2. Impact of charging protocols on cycling performance (a–c) and charge/discharge profiles (d–f) of the material tested with respective cycling protocols S, F, and S + F.

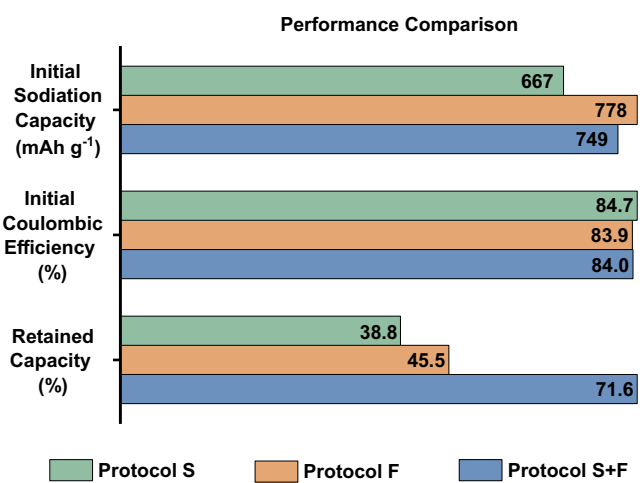


Figure 3. Comparison on the performance in terms of initial sodiation capacity, retained capacity after 100 cycles, and ICE for the three cycling protocols S, F, and S + F. ICE is obtained as the ratio of initial charge to discharge capacity and retained capacity is expressed as the ratio of the final capacity after 100 cycles to the initial sodiation capacity.

be the main focus of this work. **Figure 4** shows that the number of steps in the voltage profile varies depending on the current and/or the number of cycles. The labels and positions of characteristic plateaus are indicated here and will be used in the subsequent analysis.

Figure 2d–f depicts the different capacity–voltage profiles of the material cycled using cycling protocols S, F, and S + F, respectively. For all three of the different charging conditions, the initial cycle appears similar, with two sloping regions from around 0.28 to 0.17 V and 0.17 to 0.07 V, followed by a plateau at 0.045 V in the sodiation. At slow rates, there is a small perturbation between the sloping region and

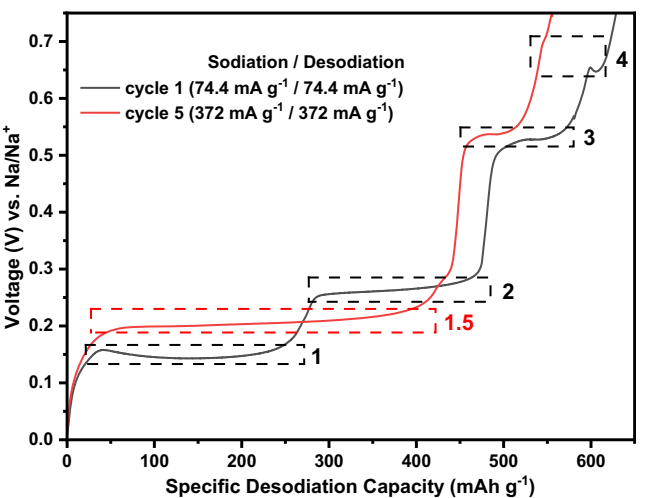


Figure 4. Impact of current density on the shape of the voltage profile. Desodiation curves for the 1st and 5th cycle using S + F settings. The figure marks the four initial dealloying plateaus, as well as plateau 1.5, which is formed by merging plateaus 1 and 2. These features will be referred in the remainder of this manuscript.

the plateau, which is absent under cycling at higher current densities. The shape of the initial desodiation curve is similar for the three tests, showing four distinct plateaus. The first plateau (**plateau 1**) is found when charging with 74.4 mA g⁻¹ at around 0.15 V, while at a higher current density of 372 mA g⁻¹, it is shifted upward to 0.17 V, possibly due to a phase-specific polarization, since not all plateaus experience this shift. The following **plateaus (2 and 3)** are located at 0.26 and 0.53 V for both current densities. The final plateau (**plateau 4**) is found at 0.65 V for slow charging and 0.69 V for higher currents.

The curves for ongoing cycling are particularly intriguing, as significant differences are observed using varying charging conditions. In Figure 2d, the initial plateaus persist at the beginning, but with continued cycling, the first and second plateaus gradually merge into a new plateau at 0.2 V. While this merging is happening, the capacity fades continuously. However, when the merging is complete and only the new plateau at 0.2 V remains, the fading slows down significantly. When higher current densities are applied, as shown in Figure 2e and f, the first two plateaus (**plateau 1** and **2**) merge within the first few cycles, forming the plateau (denoted as **plateau 1.5**). This eliminates the fading and allows the cells to provide a significantly higher capacity. While the merging of the plateaus has been reported in the literature before, it was not previously considered as a factor affecting the recovered capacity.^[15,19,21] The sample charged under the fast-charging condition exclusively (**protocol F**) (Figure 2b and e) shows this improved capacity between the 30th and 70th cycles, but the overall capacity fades due to the instability of the process while the sample cycled under the **S + F protocol** performs consistently over the whole period. From this, it can be assumed that the improvement in capacity is closely related to the formation of the new plateau at 0.2 V. Table S3 in the Supporting Information summarizes the capacities recovered by **plateau 1.5** at various cycles in absolute terms, as well as its percentage share of the capacity in the respective cycle. While the contribution of **plateau 1.5** under the **S protocol** is initially low, it is significantly higher for the other two settings, accounting for 45.9% and 43.5% for **F** and **S + F** in the second cycle, respectively. The percentage share of **plateau 1.5** increases significantly upon prolonged cycling for the slowly charged cell, indicating that this process appears to be more stable as compared to the other plateaus. This suggests that the reaction taking place at **plateau 1.5** is beneficial for the overall performance. Furthermore, for the other two cycling protocols, the contribution of this reaction also increases in both cases, making up about 50%–60% of the total capacity. Since this contribution for these two protocols is already high from the early cycles, we assume that the high currents are the driving force for the formation of this plateau. A possible explanation for its stabilization over time under slow charging conditions is the increasing current density applied to the active material. While the set current remains constant throughout the measurement, the decrease in capacity indicates a loss of active material. This reduction in active mass results in a higher effective current density on the remaining material.

The differences between the charge/discharge transients under varying charging conditions are more clearly visualized by plotting the corresponding incremental capacity curves. ICA is commonly used to study degradation mechanisms during cell aging and to analyze specific details of voltage profiles.^[22,23] It is important to note that ICA is typically conducted at very low charging rates, resulting in well-defined, high-resolution curves, as faster rates may lead to kinetic and thermodynamic effects that influence the transients. Nevertheless, ICA at faster rates can still be employed for a qualitative analysis. The IC curves exhibit slightly unusual loop-like features. Typically, there is no “overlapping,” as the voltage changes alongside the capacity.^[24] However, in this case, potential oscillations during the sodiation

and potential dips in the desodiation transient lead to irregular features in the IC curves, particularly during the initial cycles. This phenomenon is of kinetic nature and is correlated with an improved diffusion of Na ions^[14] or with the presence of small nucleation droplets and new phase formation.^[15,25] Furthermore, we consider the position of the peak maxima as features of interest (**FOI**), instead of the peak onsets, although the latter are typically used to signify the beginning of an electrochemical reaction.^[24] Figure 5 depicts the incremental capacity data retrieved from the cycling measurement using the **S + F protocol** over the first 80 cycles. The IC curves for the other measurements are shown in Figure S1 in the Supporting Information. We focus mainly on desodiation as the features are more distinctly visible; however, changes in the sodiation cannot be ignored, as desodiation processes are usually correlated with the preceding sodiation. FOI associated with the sodiation process are denoted with an “s” prefix.

During the initial sodiation, one peak is attributed to the Solid Electrolyte interface (SEI) formation, as it is exclusively observed during the initial cycle. The peak is located at 0.17 V for samples cycled with 74.4 mA g⁻¹ and at 0.15–0.16 V for the sample cycled with higher current density. A second peak, potentially also related to SEI formation, is found at 0.23 V under fast charging. However, this assignment is questionable, as the sample cycled under **S + F** conditions shows this second peak at 0.241 V in the second cycle. If this feature were entirely related to SEI formation, it would not appear in the second cycle. Instead, it suggests a reaction that specifically occurs under high current conditions. Interestingly, this feature only appears in the first cycle under high current, so it may still be attributed to an SEI-related reaction that is triggered by high current densities.

Apart from the SEI-related FOI, the slow cycling leads to a split peak in **FOI s-1** with maxima at 0.075 and 0.042 V. With prolonged cycling, the split peak at first gradually merges, subsequently forms a shoulder at lower potentials, and decreases in intensity under **protocol S**. In contrast, **FOI s-1** of the fast-cycled sample only shows a single peak at 0.047 V. **FOI s-1** is by far the most prominent sodiation feature, though other FOI can be identified upon closer inspection. **FOI s-3** is observed in all three experiments, its intensity slightly decreases during slow charging but remains stable under fast charging. More differences can be identified when looking at **FOI s-4**, under slow charging conditions, this peak disappears within a few cycles. This indicates that the reaction at this potential is suppressed, resulting in reduced capacity. At higher charging rates, this peak persists, although its intensity gradually decreases with extended cycling. Under the optimized **S + F** protocol, the peak intensifies and appears sharper than in the other cases. This may indicate that the associated reaction exhibits enhanced kinetics compared to the other protocols.

The ICA of the desodiation process conveys the same information as that shown in the charge–discharge curves. Nevertheless, ICA helps identify subtle variations within certain features that may be overlooked in the charge/discharge transients, such as possible potential shifts of specific features. High current rates cause **FOI 1** and **4** to shift toward higher potentials, indicating an increased polarization. **FOIs 1.5, 2, and 3**, on the

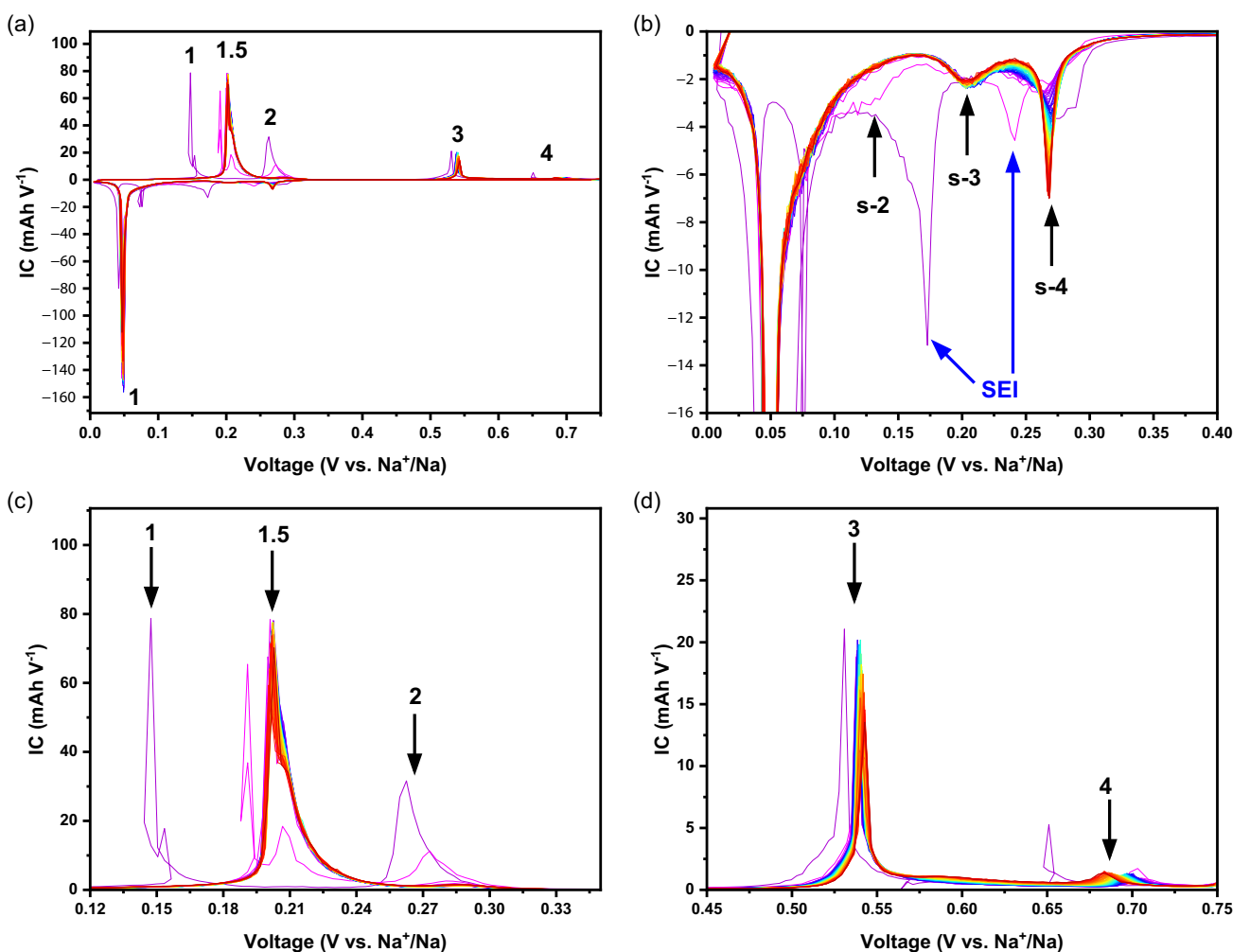


Figure 5. ICA with insets on the FOI for the charging protocol S + F. ICA with a) full cycling range and b) insets on FOI of the sodiation and c,d) insets on FOI of the desodiation.

other hand, remain largely unaffected by the increased current, inferring better kinetics for these reactions. Since the material examined with the **S + F protocol** shows the best performance, it is used as a benchmark to compare the other two samples. The cell tested with **protocol S** reveals that while **FOIs 1 and 2 merge into 1.5**, **FOI 1 shifts to higher potentials**, while the intensity of **FOI 2 decreases**. This suggests that these two reactions are linked. Since **FOI 1, 2, and 1.5 are present simultaneously**, it can be concluded that a new reaction is taking place at **FOI 1.5**. **FOI 4** of the sample cycled with **protocol F** provides insights into possible failure mechanisms of the material. During stable cycling, **FOI 4** appears as a small bump, while sharp peaks are associated to instability. In the fast-cycled sample, several spikes are observed in the range between the initial **FOI 4** and the upper cut-off potential of 0.75 V. This may indicate parasitic side reactions, possibly caused by the pulverization of Sn, which could also explain a higher desodiation capacity than sodiation capacity recorded in the GCPL. The final phase transition back to metallic Sn has been shown to be the most likely cause of material failure.^[18] In cycle 16, significant irregularities begin at the penultimate desodiation step (**FOI 3**) and continue as spikes in the IC curve toward the end

(this cycle was excluded from the insets for clarity). This again suggests pulverization of the material, exposing fresh, unreacted Sn-surface to the electrolyte. This hypothesis is further supported by observations in the subsequent cycle, 17. During sodiation, a peak at ≈ 0.14 V reappears, attributed to **SEI formation**. In the following desodiation, a peak appears around 0.182 V (between **FOIs 1 and 1.5**); interestingly, this is correlated with a higher intensity at **FOI 2**. This suggests that these reactions are coupled. Furthermore, they appear to be closely related to the renewed **SEI formation** as well. This phenomenon is depicted in Figure S2 in the Supporting Information. The plot also demonstrates that following the pronounced irregularity in cycle 16, **FOI s4** during the sodiation of cycle 17 is shifted to a higher potential and appears sharper. This indicates that desodiation affects the subsequent sodiation process. Furthermore, it is found that cycles showing efficiency over 100% due to possible side reactions all showed a peak with higher intensity at **FOI 4**, while reactions within a stable regime (cycles 31 to 68) had a small bump, similar to what was observed in the **S + F** protocol. This again indicates that this potential regime is prone to failure. In unstable cycles, **FOI 2** reappears, while in the stable regime, the intensity of **FOI 2** is

almost negligible. This behavior is depicted within Figure S3 in the Supporting Information.

In the S + F-cycled samples, which show significantly improved performance, the initial cycle matches that of the slowly cycled sample, as expected. The second cycles (corresponding to the first application of a high current density) closely resemble the second cycle of the sample charged solely with high current density. FOI 2 is observed in the initial cycle and second cycle but basically disappears thereafter. FOI 4 forms the small bump earlier than in the sample charged only with high current densities. During prolonged cycling, FOI 1 disappears, while FOI 1.5 stabilizes at 0.2 V, maintaining its position and intensity, indicating stable cycling. The same can be said for FOI 3, which retains its position after the second cycle. The peak decreases slightly in intensity initially but stays constant afterward. FOI 4 exhibits a slight shift toward lower potentials during prolonged cycling, which may be due to a reduced effect of polarization.

While the S + F protocol clearly improves the performance of the C/Sn electrode, the reason behind it is not straightforward. A possible explanation may be that the slow charging rates are forming a more stable SEI, which is able to accompany the volume changes during the charging or discharging better, thereby suppressing side reactions. However, this cannot be the sole reason for enhanced performance as the cell cycled, using protocol S, should then show the same behavior. Instead, the combination of slow initial currents for the formation of a stable SEI, together with high currents in subsequent cycles, opening up an improved reaction pathway, is essential. Further research is crucial to provide a clear answer on how the improvement is achieved, including operando or postmortem analysis of cells cycled under different conditions.

Palaniselvam et al.^[19] also investigated the phenomena of charging conditions influencing the process. They described a memory effect, suggesting that the conditions applied during sodiation determine the number of plateaus during charging. In their study, they applied asymmetric cycling conditions, either performing sodiation at high (500 mA g^{-1}) and the desodiation at low current density (50 mA g^{-1}), or vice versa. We also tested asymmetric charging as well, but with an additional formation cycle at 74.4 mA g^{-1} prior to the asymmetric protocol, and employed 74.4 mA g^{-1} as the low and 372 mA g^{-1} as the high current density. Figure 6 shows the resulting cycling performance, charge/discharge profiles, and ICA. The material sodiated slowly and desodiated rapidly (Figure 6a–c), referred to as Asy. SF indeed exhibits similarities in its desodiation behavior to the material cycled entirely at slow current rates during the initial cycles. With prolonged cycling, the desodiation plateaus 1 and 2 merge. The incremental capacity curve of the desodiation shows peaks from the second cycle onward at around 0.165 V, gradually shifting with prolonged cycling toward FOI 1.5, similar to the cell cycled with the protocol S. The peak is slightly shifted toward higher potentials, which may be due to polarization induced by the higher current rate. FOI 1.5 and 2 exhibit similar shifts. FOI 3 partly mirrors the desodiation behavior of the slowly cycled cell, also showing decreasing peak intensity. Interestingly, an additional peak is formed with extended cycling at 0.58 V, which is also absent in the fast-cycled sample. This suggests that the desodiation process is not entirely correlated to the preceding sodiation current. However, since its behavior also differs from that observed in the fast-cycled cell, it is evident that adjusting the cycling parameters significantly impacts the desodiation mechanism, further highlighting the complexity of this process. FOI 4 is comparable to that observed in the slow-cycled cell, but is shifted to higher

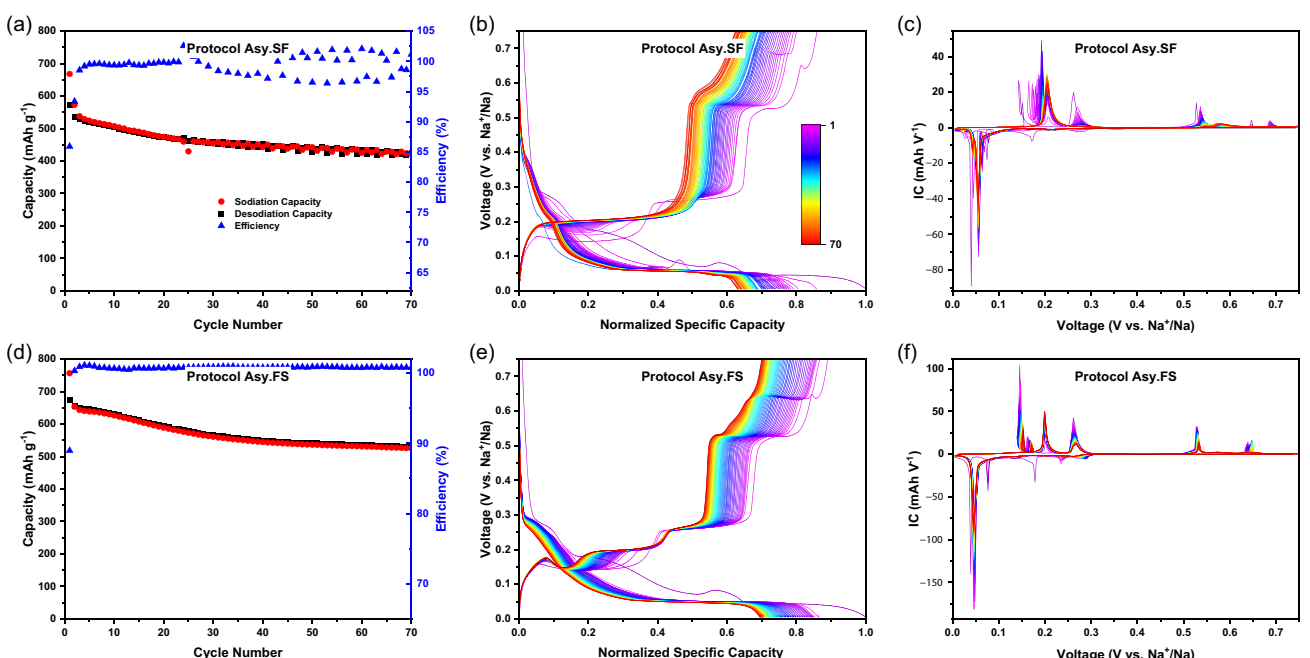


Figure 6. Asymmetric cycling test with the initial cycle carried out using a low current of 74.4 mA g^{-1} . a,d) cycling performance, b,e) charge/discharge curves, c,f) ICA using slow (74.4 mA g^{-1}) discharge and fast (372 mA g^{-1}) charge, and fast discharge and slow charge, respectively.

potentials, again likely due to polarization effects. This may indicate that the process corresponding to FOI 4 is more closely related to the sodiation parameters than to the desodiation conditions.

When the asymmetric cycling is switched to high currents (372 mA g^{-1}) for sodiation and low currents (74.4 mA g^{-1}) in the desodiation (Asy. FS), the reported memory effect is not observed. The resulting cycling performance, charge/discharge, and ICA curves are displayed in Figure 6d-f. The charge/discharge profiles show a different progression compared to all the previous experiments. The desodiation branch shows that under these specific charging parameters, the first plateau and following potential dip sustain for a longer time, and the plateau at 0.2 V is gradually being formed within each subsequent cycle. Interestingly, even though the capacity provided by the first plateau decreases with each cycle, it is fully recovered with the formation of **plateau 1.5**, when reaching 0.25 V . Only after this point does capacity fading occur, suggesting that the capacity loss is primarily associated with the phase transition at **plateau 2**. In other words, this means that the combined capacity of **plateau 1** and **plateau 1.5** remains constant, whereas at slow rates (**S protocol**), capacity loss also occurs with the formation of **plateau 1.5**. Furthermore, this cycling procedure supports our hypothesis that the presence of **plateau 1 and 2** is correlated, as both persist throughout the test. Additional capacity loss occurs up to **plateau 3** (0.60 V), which stays constant after **plateau 4** (0.70 V). Additionally, the shape of the desodiation curve remains constant with well-defined **plateaus 3 and 4**. ICA confirms these findings, showing two sharp peaks at 0.53 and 0.65 V corresponding to **plateaus 3 and 4**, respectively, which retain their positions and slightly decrease in intensity during cycling. Furthermore, an anomaly is identified within the IC curve, namely the presence of two peaks at **FOI 1**. This can be explained

by the shape of the desodiation profile in Figure 6e. Due to the voltage dip before **plateau 1**, multiple capacity values can be attributed to a single potential, leading to the irregular shape of the IC curve. In an ideal charging scenario, the voltage steadily increases with increasing charge storage, which is not the case here. If this voltage dip is associated with the formation of nucleation droplets, the two peaks observed here can most likely be attributed to one reaction and not two separate ones. In the sodiation transient, a peak at 0.234 V is registered. This feature was observed prior in the cells cycled with the **F** and **S + F** protocols, the compelling difference, however, is that in these cases, the peak was only observed once when the high current was applied for the first time. In the case of asymmetric cycling, this peak reappears for several cycles. Finding a clear explanation for this behavior remains difficult. We allow ourselves to speculate that this process occurs at fast sodiation rates and might gain some reversibility when the desodiation is carried out slowly, but when desodiation is carried out at high currents, this process remains irreversible. Furthermore, the peak at 0.234 V is absent, once the sodiation is performed at low current and the desodiation at fast current. Therefore, this feature should be associated with fast discharge currents.

To gain further insights into the merging of **plateaus 1 and 2**, two additional GCPL measurements were conducted, in which the cut-off potentials were adjusted to 0.05 V in the sodiation or 0.23 V in the desodiation to remove **plateau 1 or 2**, respectively, from the desodiation profile. Figure 7a-c displays GCPL data with the lower cutoff potential set to 0.05 V . Applying this lower limit excludes the final sodiation plateau, and consequently, the first desodiation plateau is also absent in the initial cycle. The remaining desodiation curve is identical to previous measurements. Interestingly, in the following cycles, the shape

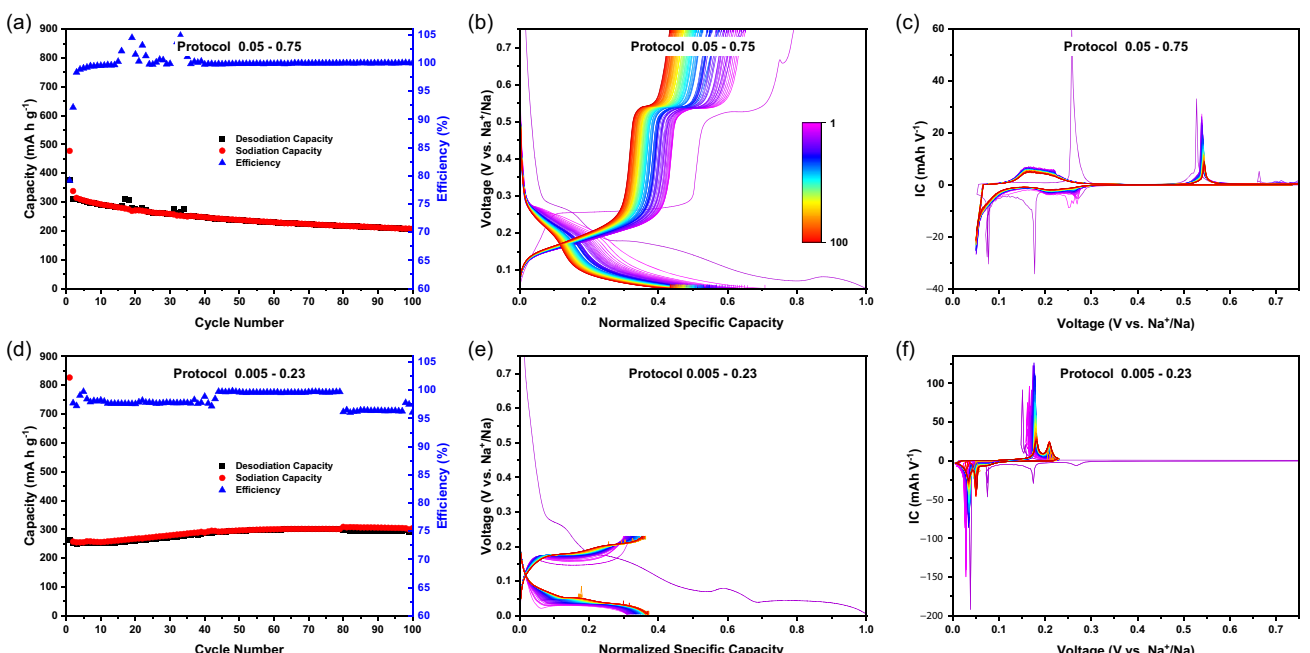


Figure 7. a,d) Impact of altered cut-off potentials on the cycling performance, b,e) charge/discharge profiles, and c,f) ICA, respectively, for a discharge limit of 0.05 V or a charge limit of 0.23 V . The initial cycle was carried out at low current densities of 74.4 mA g^{-1} and subsequent cycles with 372 mA g^{-1} .

changes significantly. Instead of a distinct **plateau 2**, a sloping region is observed, with an onset at around 0.12 V until 0.26 V. Analogously, the ICA shown in Figure 7c reveals a sharp peak at around 0.258 V in the initial cycle, which disappears upon further cycling and evolves into a broad hump, indicative of a solid solution process, whereas the presence of a peak is characteristic for a phase transformation.^[24] It is important to note that the initial cycle was recorded at a formation current density of 74.4 mA g⁻¹, while subsequent cycles were conducted at higher currents following the **S + F protocol**. To determine whether this behavior is related to the higher current, the same test was repeated using faster charging rates from the beginning. No plateau forms in the initial cycle, indicating that this process is directly correlated with the applied charging rate. The results of the measurements conducted without a formation cycle are shown in the Supporting Information in Figure S4. Since the regime investigated in this experiment represents a subregime of the one used during **S + F** testing, it would be reasonable to assume a similar process stability. However, this is not the case; instead, significant capacity fading occurs. These observations lead to several hypotheses. First, the reaction taking place here

seems to be unfavorable for the performance. Additionally, it can be inferred that the desodiation reaction differs from that observed under **S + F** conditions. This means the desodiation does not simply begin from a different starting point, while following the same path. Instead, it appears that complete sodiation enables an alternative desodiation pathway, with improved reversibility. Another interesting observation is that the onset of this new reaction occurs at an even lower potential than that of **plateau 1**. This reaction, therefore, seems to occur only when it is isolated; otherwise, it would also appear in the other experiments. In other words, the preceding sodiation state appears to determine how desodiation proceeds. This reaction, therefore, seems to occur only when it is isolated; otherwise, it would also appear in the other experiments. In other words, the preceding sodiation state appears to determine how desodiation proceeds. **FOI 4** disappears rapidly under these charging conditions.

In the next step, the behavior of **plateau 1** in isolation was investigated. Figure 7d-f shows the cycling performance, charge/discharge curves, and ICA for an upper cut-off potential of 0.23 V, which lies below the formation potential of **plateau 2**. In this case, during desodiation, **plateau 1** forms in the initial

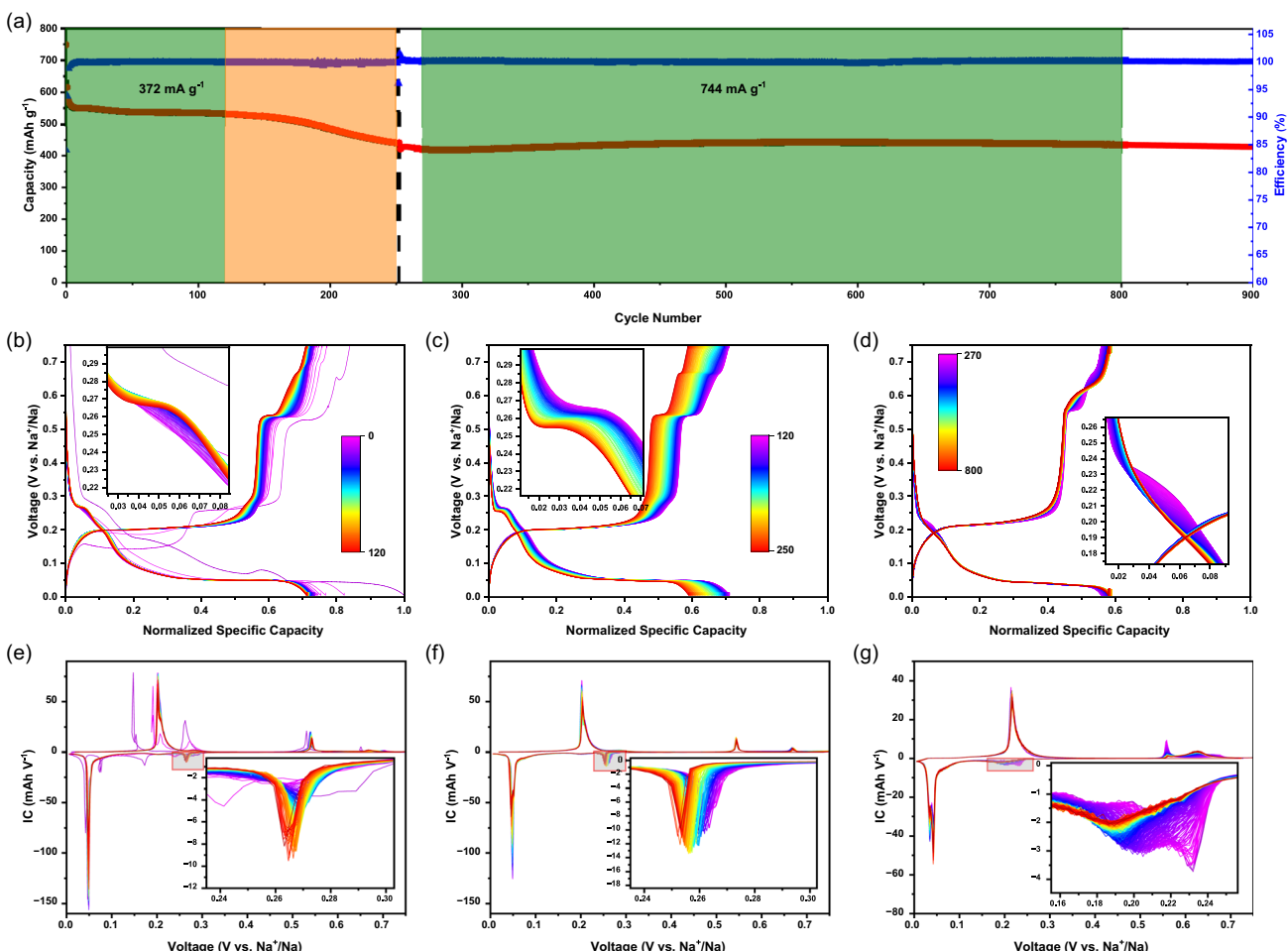


Figure 8. Long-term cycling performance of the cell tested via the **S + F** protocol. a) Cycling performance. The green areas mark regimes with stable cycling performance (cycle 0–120 and 270–800) and the orange area marks a regime, where capacity fading occurs (cycle 120–250). b–d) respective charge/discharge transients, and e–g) respective ICA. Insets represent regions which may be associated with stability or instability.

cycle, and the overall shape of the charge/discharge curve remains the same after prolonged cycling. Upon reaching potentials above 0.2 V, the capacity increases with cycling, suggesting that processes related to **plateau 1.5** may already be occurring, even though the original position of **plateau 1** remains unaffected. This is also observed in the IC curve with a gradually growing peak at 0.2 V. No capacity fading is observed here, underlining the stability of this reaction process. One might assume that under these charging parameters, the entire plateau shifts to 0.2 V as in the **S + F** process and the merging of the plateaus occurs because the upper cut-off lies above the potential for **plateau 1.5**. However, this is not the case. Instead, it appears that the presence of **plateau 2** is necessary for the full shift or merging to occur. There are also no significant differences when switching from slow to fast current rates, suggesting that the current rate does not influence this reaction. Figure S4 depicts the charge/discharge curve obtained by the same experiment without the slow formation cycle, confirming that the differences between fast and slow cycling conditions are negligible. In summary, desodiation at **plateau 2** primarily contributes to the capacity loss and is more sensitive to increased current rates.

Finally, the long-term cycling stability using the best-performing **S + F protocol** is evaluated. Therefore, cycling of the cell was continued for over 900 cycles. Two different current densities were applied, first 372 mA g^{-1} , then 744 mA g^{-1} . The results are depicted in **Figure 8**. At around 120 cycles, a noticeable capacity drop was observed (highlighted in the orange area of Figure 8). After switching to a higher current rate, stable performance was regained.

In Figure 8a, the cycling performance is divided into three sections, cycles 1–120, 120–250, and 270–800, respectively. The first section illustrates the initially stable performance, the second captures the period of capacity fading, and the last section shows the stabilized performance following the current increase. A closer look at the charge/discharge curve in Figure 8b shows the gradual formation of an additional step at around 0.55 V after continued cycling, where previously a sloping region was present. This feature becomes more pronounced in the middle section (Figure 8c), suggesting its potential link to the observed capacity decay. The formation of this feature is well visible in the corresponding ICA curves. In Section 1 (Figure 8e), a peak in the cathodic branch forms between 0.26 and 0.27 V, which gradually shifts toward lower potential and becomes sharper as cycling progresses. In section 2 (Figure 8f), with increasing fading, this peak moves further toward lower potentials and becomes sharper. The shift toward lower potential might be correlated to an amplified polarization resistance induced by the increased current. After increasing the current, this feature is no longer observed; instead, the charge/discharge and ICA curve at this potential more closely resemble the initial curves of Section 1. Since the material exhibits stable performance in Section 3 (Figure 8d and g) once again, it can be hypothesized that the appearance of this feature may serve as an early indicator of performance degradation. The fact that an alteration of the charging parameters led to performance restabilization suggests a potentially effective strategy for delaying cell ageing, provided these features are closely monitored.

4. Conclusion

This study addresses the influence of varying charging parameters on the electrochemical performance of a synthesized C/Sn composite anode material for SIB. The results demonstrate that although higher current rates may lead to parasitic side reactions or pulverization, they can be beneficial in terms of achievable capacity. Optimal performance is achieved when the initial cycle conducted at low currents and prolonged cycling is realized under higher current rates. In this way, the capacity improved from 259 mAh g^{-1} up to 536 mAh g^{-1} after 100 cycles, with an excellent mean efficiency of 99.82%.

The enhanced performance is strongly correlated with the emergence of a new desodiation process at 0.2 V, when applying high currents. This is evidenced by the merging of two original plateaus in the desodiation curve into a single new plateau. This new plateau at 0.2 V leads to a stable capacity, while the other processes often result in capacity fading. Asymmetric cell cycling further emphasizes the complexity of the alloying process between Na and Sn, as not only the current rate in the desodiation needs to be considered, but also the current rate of the preceding sodiation affects the following process. For instance, fast discharge, followed by slow charge, reveals that capacity fading occurs only at potentials higher than that of the new desodiation process described above.

Adjusting the cut-off potential reveals further information about the effect of specific reactions on electrochemical behavior. An upper cut-off voltage of 0.23 V primarily leads to the presence of the first original plateau within the charge transient and is barely influenced by an increased current rate and shows very good reversibility. On the other hand, limiting the sodiation to 0.05 V removes this first desodiation step from the desodiation branch and the second desodiation plateau shows a significantly different behavior. This process in turn is heavily dependent on the applied current and the desodiation profile changes from a plateau to a sloping region, accompanied by capacity fading.

The long-term performance of the optimized **S + F** protocol shows stable performance over 900 cycles. Early indications of cell degradation are identified, along with the possibility of restabilizing the cell by altering the charging currents.

The findings in this work highlight the crucial role of optimized charging protocols in achieving superior performance of Sn-alloy-based anodes, providing valuable insights for the future design of SIB with enhanced longevity and efficiency. In particular, the merging of plateaus 1 and 2 into a single plateau at 0.2 V (**plateau 1.5**), enabled by fast-charging rates, emerges as a key factor for optimal performance. Additionally, implementing a formation cycle at low current density significantly enhances cyclability, while ensuring complete sodiation contributes to the stability of the achievable capacities.

Acknowledgements

The authors gratefully acknowledge the financial support by the German Research Foundation (DFG) in the frame of the BEETHOVEN Classic 3 – Polish-German Funding Initiative

(GR 4440/4-1) and the EU project SIMBA (sodium-ion and sodium metal batteries for efficient and sustainable next-generation energy storage) under grant agreement number 963542.

Open Access funding enabled and organized by Projekt DEAL.

Conflict of Interest

The authors declare no conflict of interest.

Data Availability Statement

The data that support the findings of this study are available in the supplementary material of this article.

Keywords: alloy-based anodes · sodium-ion batteries · tin

- [1] C. Marino, J. Cabanero, M. Povia, C. Villevieille, *J. Electrochem. Soc.* **2018**, *165*, A1400.
- [2] A. Kamiyama, K. Kubota, D. Igarashi, Y. Youn, Y. Tateyama, H. Ando, K. Gotoh, S. Komaba, *Angew. Chem., Int. Ed.* **2021**, *60*, 5114.
- [3] A. Kamiyama, K. Kubota, T. Nakano, S. Fujimura, S. Shiraishi, H. Tsukada, S. Komaba, *ACS Appl. Energy Mater.* **2020**, *3*, 135.
- [4] X. Dou, I. Hasa, D. Saurel, C. Vaalma, L. Wu, D. Buchholz, D. Bresser, S. Komaba, S. Passerini, *Mater. Today* **2019**, *23*, 87.
- [5] S. Mukherjee, S. Bin Mujib, D. Soares, G. Singh, *Materials* **2019**, *12*, 1952.
- [6] Z. Li, J. Ding, D. Mittlin, *Acc. Chem. Res.* **2015**, *48*, 1657.
- [7] M. Lao, Y. Zhang, W. Luo, Q. Yan, W. Sun, S. X. Dou, *Adv. Mater.* **2017**, *29*, 1700622.
- [8] X. Du, Y. Gao, Z. Hou, X. Guo, Y. Zhu, B. Zhang, *ACS Appl. Energy Mater.* **2022**, *5*, 2252.

- [9] B. Zhang, G. Rousse, D. Foix, R. Dugas, D. A. D. Corte, J.-M. Tarascon, *Adv. Mater.* **2016**, *28*, 9824.
- [10] A. Kempf, S. Kiefer, M. Graczyk-Zajac, E. Ionescu, R. Riedel, *Open Ceram.* **2023**, *15*, 100388.
- [11] Y. Liu, Y. Xu, Y. Zhu, J. N. Culver, C. A. Lundgren, K. Xu, C. Wang, *ACS Nano* **2013**, *7*, 3627.
- [12] F. Jiang, F. Luo, Q. Fan, P. Guo, Y. Liao, M. Chen, C. Liu, J. Chen, D. Wang, Z. Zheng, *J. Electroanal. Chem.* **2024**, *959*, 118186.
- [13] V. L. Chevrier, G. Ceder, *J. Electrochem. Soc.* **2011**, *158*, A1011.
- [14] L. D. Ellis, T. D. Hatchard, M. N. Obrovac, *J. Electrochem. Soc.* **2012**, *159*, A1801.
- [15] L. Baggetto, P. Ganesh, R. P. Meisner, R. R. Unocic, J.-C. Jumas, C. A. Bridges, G. M. Veith, *J. Power Sources* **2013**, *234*, 48.
- [16] L. Baggetto, C. A. Bridges, J.-C. Jumas, D. R. Mullins, K. J. Carroll, R. A. Meisner, E. J. Crumlin, X. Liu, W. Yang, G. M. Veith, *J. Mater. Chem. A* **2014**, *2*, 18959.
- [17] J. M. Stratford, M. Mayo, P. K. Allan, O. Pecher, O. J. Borkiewicz, K. M. Wiaderek, K. W. Chapman, C. J. Pickard, A. J. Morris, C. P. Grey, *J. Am. Chem. Soc.* **2017**, *139*, 7273.
- [18] Y. Zhu, Z. Qian, J. Song, W. Du, J. Pan, D. Wang, J. Yang, *Nano Lett.* **2021**, *21*, 3588.
- [19] T. Palanisvam, M. Goktas, B. Anothumakkool, Y.-N. Sun, R. Schmuck, L. Zhao, B.-H. Han, M. Winter, P. Adelhelm, *Adv. Funct. Mater.* **2019**, *29*, 1900790.
- [20] A. Kempf, M. Graczyk-Zajac, R. Riedel, *ACS Materials Lett.* **2025**, *7*, 275.
- [21] C. Kim, I. Kim, H. Kim, M. K. Sadan, H. Yeo, G. Cho, J. Ahn, J. Ahn, H. Ahn, *J. Mater. Chem. A* **2018**, *6*, 22809.
- [22] L. Spithhoff, P. J. Vie, M. S. Wahl, J. Wind, O. S. Burheim, *J. Electroanal. Chem.* **2023**, *944*, 117627.
- [23] S. Lochab, S. Bharathraj, K. S. Mayya, P. Barpanda, S. P. Adiga, *Batteries Supercaps* **2024**, *7*, e202400025.
- [24] M. Dubarry, D. Anseán, *Front. Energy Res.* **2022**, *10*, 1023555.
- [25] M. D. Levi, D. Aurbach, *J Solid State Electrochem* **2008**, *12*, 409.

Manuscript received: May 5, 2025

Revised manuscript received: June 27, 2025

Version of record online: